Debye scale turbulence within the electron diffusion layer during magnetic reconnection

J. Jara-Almonte,[1] W. Daughton,[2] and H. Ji[1]
[1]Center for Magnetic Self-Organization, Max-Planck/Princeton Center for Plasma Physics, Princeton Plasma Physics Laboratory, Princeton, New Jersey 08543, USA
[2]Los Alamos National Laboratory, Los Alamos, New Mexico 87545, USA

(Received 6 January 2014; accepted 25 February 2014; published online 18 March 2014)

During collisionless, anti-parallel magnetic reconnection, the electron diffusion layer is the region of both fieldline breaking and plasma mixing. Due to the in-plane electrostatic fields associated with collisionless reconnection, the inflowing plasmas are accelerated towards the X-line and form counter-streaming beams within the unmagnetized diffusion layer. This configuration is inherently unstable to in-plane electrostatic streaming instabilities provided that there is sufficient scale separation between the Debye length λ_D and the electron skin depth c/ω_{pe}. This scale separation has hitherto not been well resolved in kinetic simulations. Using both 2D fully kinetic simulations and a simple linear model, we demonstrate that these in-plane streaming instabilities generate Debye scale turbulence within the electron diffusion layer at electron temperatures relevant to magnetic reconnection both in the magnetosphere and in laboratory experiments. © *2014 AIP Publishing LLC*. [http://dx.doi.org/10.1063/1.4867868]

I. INTRODUCTION

Magnetic reconnection is the fundamental process wherein magnetic fieldlines break and release stored magnetic energy into plasma kinetic energy.[1] Despite its prevalence, magnetic reconnection is not well understood and remains one of the most perplexing problems in plasma physics. Due to the predictive capabilities of modern computer simulations and thorough measurements of reconnection layers both in laboratory experiments and in the magnetosphere, significant progress has been made toward understanding 2D collisionless reconnection. The decoupling of the ions and electrons at scales below the ion skin depth allows for fast reconnection in both fluid and kinetic models,[2] suggesting that ion physics determines the reconnection rate, despite electron physics being fundamentally responsible for the fieldline breaking. Ion scale reconnection physics is well studied, and good agreement between simulations and experiments has been reported.[3–7]

In contrast, on electron scales there remain significant discrepancies between simulations and experiments on both the structure of and force balance within the electron diffusion layer.[8] These discrepancies cannot be explained by either finite collisionality or anomalous resistivity generated by lower-hybrid drift instability (LHDI) turbulence.[7,9] In experiments, the physical process responsible for setting the width of the electron diffusion layer has not been identified despite significant effort. This suggests that it operates on scales beyond the resolution of current diagnostics, effectively limiting it to length scales equal to or smaller than the electron skin-depth or frequencies greater than the lower-hybrid frequency. One such possible mechanism is the presence of many small-scale flux ropes within the electron diffusion layer.[6,10] Recent measurements have observed flux ropes on scales below the current sheet width,[7] however, there are no measurements that conclusively show that volume-filling flux-ropes are the cause of the broad electron diffusion layer observed.

Reports of the electron diffusion layer width from *in-situ* observations are limited due to infrequent electron diffusion layer crossings and the low time resolution of instruments on current spacecraft. One such report[11] seems to support the simulation predictions of a thin electron diffusion layer, however, others suggest a broader diffusion layer more consistent with experimental observations.[12] With the upcoming launch of the Magnetospheric Multiscale Mission (MMS), better time resolution and more electron diffusion layer encounters will provide a clearer understanding of the structure of the electron diffusion layer in the magnetosphere.[13]

Because of these outstanding discrepancies, the approximations used in present day kinetic simulations of reconnection must be examined. Of the few approximations imposed, the only one which, to date, has not been seriously examined is the artificially low ratio of the speed of light to the electron thermal speed, c/v_{the}, used. This parameter sets the scale separation between the electron skin-depth and the Debye length, $c/v_{the} = d_e/\lambda_D$ and so controls the coupling of Debye scale and skin-depth scale physics. Validation of kinetic codes has justified the low c/v_{the} approximation for studying ion scale dynamics, however, this approximation is still used even when studying electron scale dynamics which could, in principle, be strongly affected by Debye scale physics.

On the Debye scale, perhaps the most important physical processes are the streaming instabilities including, for example, the electron two-stream instability or the Buneman instability.[14] The relationship between the various linear instability branches for two counter-streaming populations has been summarized in the literature.[15] In the context of reconnection theory, Che *et al.*[16] have discussed the growth of Buneman instability within the electron diffusion layer due to strong parallel streaming in the presence of a guide field, and Goldman *et al.*[17] have discussed the generation of

electron holes along the separatricies, again due to parallel streaming in the presence of a guide field.

Electron holes are long-lived nonlinear structures which represent a solitary solution to the Vlasov-Poisson system. During magnetic reconnection, laboratory experiments have observed electron holes in the presence of a strong guide field.[21] During anti-parallel reconnection, an electric field inversion layer embedded within the unmagnetized electron diffusion layer, along with an associated electron hole, was identified by Chen.[22] This hole is an intrinsic feature of the current sheet and thus is very different than traditional instability-driven holes.

Typically, semi-implicit or explicit kinetic codes adopt $c/v_{the} \sim 10$ due to the significant reduction in computational cost that this allows. Recent work with a fully implicit code[23,24] has allowed for this parameter to be higher, $c/v_{the} \sim 20$–30, but also used extremely large cell sizes and time steps such that Debye scale physics is not resolved.

In addition to reconnection physics, detailed electron kinetics within current sheets are important in understanding the dissipation processes in large-scale collisionless turbulence. In particular, large scale kinetic simulations have suggested that in 2D collisionless turbulence, thin current sheets are the primary sites of dissipation.[25] As with reconnection simulations, these kinetic simulations use an artificially high electron temperature, so that Debye scale physics is eliminated within the current sheets.

Here, we perform the first detailed study of the role of Debye scale physics on the structure of the electron diffusion layer in 2D anti-parallel reconnection. Resolving the scale separation between the Debye scale and the skin depth allows an instability to grow which breaks the electric field inversion layer down into multiple Debye scale holes. These secondary electron holes interact nonlinearly to drive turbulence within the diffusion layer. This is fundamentally different than the laminar model typically associated with the electron diffusion layer, however, in 2D this turbulence cannot directly affect the large scale reconnection physics. In 3D, it is possible that this turbulence could generate anomalous resistivity either directly or through secondary instabilities such as the formation of small-scale flux ropes.

II. SIMULATION PARAMETERS

In order to study the regime of large c/v_{the}, several 2D, fully kinetic, collisionless simulations were done using an existing electromagnetic PIC code[26] either using the Harris equilibrium in a periodic box, or using the global Magnetic Reconnection Experiment (MRX) geometry.[5,27] The MRX geometry is a 2D driven system designed to model the MRX.[28] Unlike the Harris equilibrium, no current sheet is initially imposed such that the resulting current sheet is formed entirely by the drive scheme employed.

In both geometries, both the initial ratio of plasma to magnetic pressure, $\beta \equiv 8\pi nT/B_0^2$, and the ratio of ion to electron temperature T_i/T_e are held fixed. This implies that changing c/v_{the} is equivalent to changing the frequency ratio ω_{pe}/Ω_e. Typical values for these parameters at sites of reconnection are listed in Table I. In order to study the fundamental physics introduced by changing the scale separation, we consider only the idealized case of collisionless, anti-parallel reconnection with equal ion and electron temperatures, $T_i/T_e = 1$.

TABLE I. Typical electron density, reconnecting magnetic field strength, and upstream electron temperature for sites of magnetic reconnection, as well as the key dimensionless parameters associated with these quantities. Adapted from Ji and Daughton[20] and references therein, as well as the *in-situ* observations referenced.

	n_e [cm^{-3}]	B [nT]	T_e [eV]	ω_{pe}/Ω_e	c/v_{the}
Magnetotail[18]	0.1–1	10	100–1000	10–30	20–70
Magnetopause[11]	10–20	20–100	100–300	10–70	40–70
Solar Corona	10^{10}	2×10^7	200	1–2	50
Solar wind[19]	10–20	5–10	12	100–150	200
MRX	$(1–10) \times 10^{13}$	2×10^7	5–10	50–200	220–320
Typical PIC				<10	10

The Courant-Friedrichs-Lewy condition is a severe restriction on the allowable timesteps in the large c/v_{the} limit, so a semi-implicit algorithm was used to solve Maxwell's equations.[26,29] In order to resolve all plasma physics, timesteps, Δt, were chosen such that $\Delta t\, v_{the} \approx 0.175\Delta x$, and, with the exception of case 7, cell sizes were chosen such that Debye scale physics is well resolved, $\Delta x = 0.8\lambda_D$ for cases 1–4.

For the Harris sheet cases, we consider only anti-parallel reconnection, such that in our coordinate system the initial magnetic field is given by $B_z = B_0 \tanh(x/L)$, where L is the initial current sheet thickness. The initial temperature profile is uniform, and so to ensure force balance, the initial density profile is given by $n = n_0 \operatorname{sech}(x/L)^2 + n_b$. Length scales are normalized to the initial electron skin depth $d_{e0} = c/\omega_{pe0}$, where $\omega_{pe0}^2 = 4\pi n_0 e^2/m_e$, and time is normalized by the initial upstream ion cyclotron frequency $\Omega_{i0} = eB_0/m_i c$. For the cases considered here, the simulation domain is $10d_{i0} \times 20d_{i0}$ with periodic boundary conditions in z and conducting walls in x. The upstream density is fixed at $n_b/n_0 = 0.3$. Finally, in order to seed single X-line reconnection, an initial long wavelength perturbation was also applied.

For the MRX geometry, details of the drive scheme and boundary conditions are given in Dorfman *et al.*[5] The initial equilibrium is uniform in both density and temperature, with the magnetic field profile given by the vacuum field solution for the two flux-core coils inside of the perfectly conducting box. The length scales, normalized to the initial ion skin-depth, are matched to the actual MRX experiment, and the time is normalized by the initial ion cyclotron frequency, with the magnetic field measured at $Z_0/2$ upstream of the X-point. Here Z_0 denotes the separation between the two surfaces of the flux cores, which with our choice of parameters is given by $Z_0 = 7.8d_{i0}$. The drive time is fixed at $\tau\Omega_{i0} = 150$, such that the ratio of Alfvén time to drive time is given by $\tau_A/\tau = 0.052$. Finally, for all but one case presented here, the mass ratio is $m_i/m_e = 25$. A summary of all relevant parameters is given in Table II.

III. DEBYE SCALE INSTABILITIES

Before discussing the electron physics in detail, we first demonstrate that introducing significant scale separation

TABLE II. Simulation parameters for the cases presented here.

Number	Geometry	L_x/d_i	L_z/d_i	$\Delta x/\lambda_{De0}$	$\Delta z/\lambda_{De0}$	Particles	m_i/m_e	T_i/T_e	n_b/n_0	ω_{pe}/Ω_e	c/v_{the}
1	Harris	10	20	0.8	0.8	3.5×10^8	25	1	0.3	4	8
2	Harris	10	20	0.8	0.8	1.4×10^9	25	1	0.3	8	16
3	Harris	10	20	0.8	0.8	5.6×10^9	25	1	0.3	16	32
4	Harris	10	20	0.8	0.8	2.2×10^{10}	25	1	0.3	32	64
5	MRX	15	30	1	1	10^9	25	1	…	1	8
6	MRX	15	30	1.6	1.6	3.6×10^{10}	25	1	…	8	64
7	MRX	15	30	2.5	2.5	9×10^9	100	1	…	8	62

between the Debye length and the electron skin-depth causes a significant qualitative change in the internal structure of the electron diffusion layer. In Figure 1, the structure of the electron diffusion layer in cases 5 and 6 is compared. The only parameter changed between these two simulations is the ratio of the electron skin depth to the Debye length, or equivalently the electron temperature $d_e/\lambda_D = c/v_{the}$. Clearly, changing the scale separation has introduced new physics which breaks the laminar structure of the electron diffusion layer. Key observations about the observed small scale structures are:

1. The observed electrostatic structures are Debye scale. Above a critical value of c/v_{the}, these structures are observed, and the typical wavenumbers are in the range $k_x\lambda_D = 0.1$–0.3. This suggests that their linear origin must be an electrostatic instability.
2. The structures are nonlinear electron holes.[22] As can be seen in the phase space contours of Figure 1, there are phase space holes within the diffusion layer. These electron holes create the series of potential hills shown in the upper panels of the same figure.
3. The electron holes are dynamic and interact with each other to generate microturbulence within the diffusion layer. Typical amplitudes of these electron holes are on the order of $e\phi/T_{e0} \sim 1$, and particle trapping can cause density perturbations up to $\delta n/n \sim 1$. This is qualitatively different than the stationary electrostatic structures observed at low c/v_{the}, which have been previously reported.[22]
4. The fluctuations associated with the electron holes are nonlinearly electromagnetic. Particle trapping due to the intense electric fields generated by these electron holes and subsequent acceleration by the reconnection electric field leads to significantly enhanced current density in localized regions. Locally, the current density can be enhanced by as much as a factor of 2, as will be discussed in Sec. VI B.
5. There are two distinct modes present within the diffusion layer as shown in Figure 1(c). In addition to the electron holes, a fast mode propagating predominantly in the outflow direction is also present within the diffusion layer.

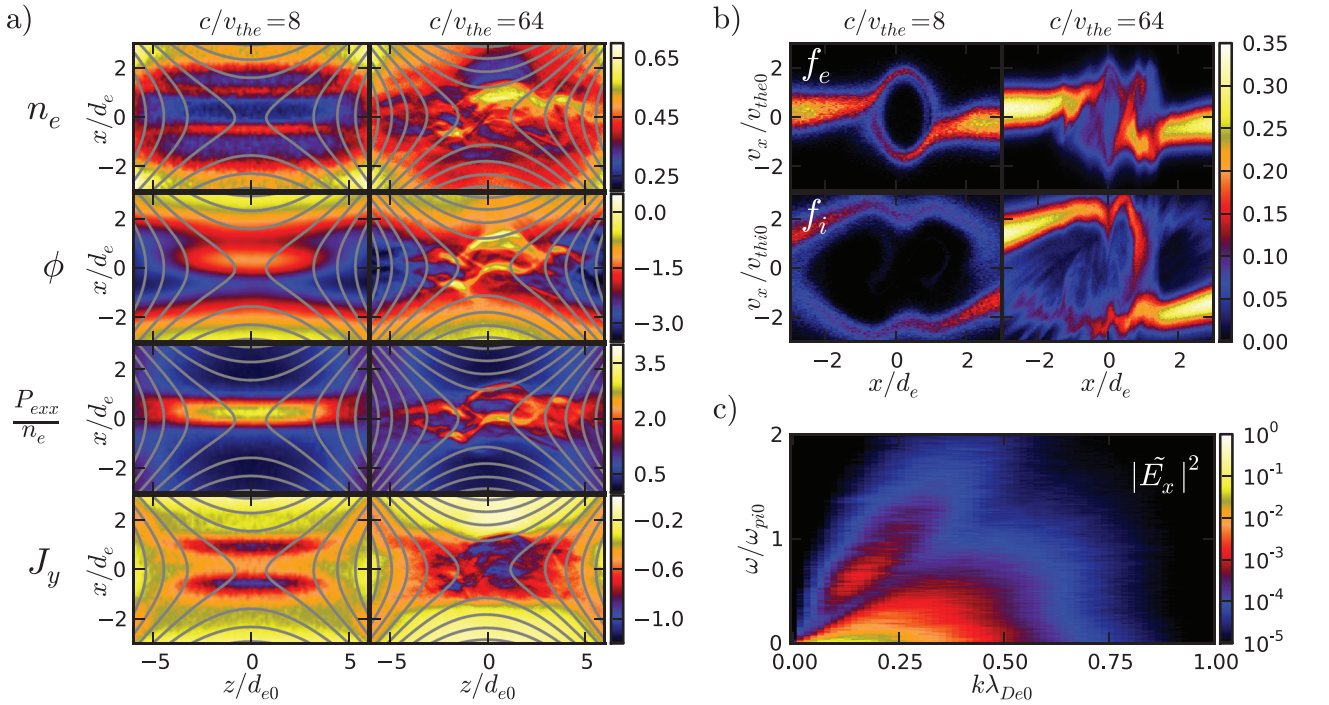

FIG. 1. Comparison between cases 5 and 6. A distinct qualitative change is seen in both (a) fluid variables and (b) reduced phase space at $z=0$ due to the introduction of Debye scale physics. The normalizations used are n_e/n_0, $e\phi/T_{e0}$, P_{exx}/n_eT_{e0}, and J_y/en_0v_{the0}. Particle distribution functions are integrated over $\pm 1d_e$ in $\hat{z}$. (c) The electric field fluctuation spectrum in case 6, normalized to the peak power.

For the parameter regime studied here, this mode is not the dominant mode and so will not be discussed further.

In the following sections, we will demonstrate that this new instability is a general feature of collisionless, anti-parallel reconnection, independent of simulation geometry and fundamentally arises due to the in-plane motion of both electrons and ions.

IV. MULTISTREAM INSTABILITIES

When there is not a significant separation between the Debye length and the electron skin depth, the meandering orbits of the inflowing electrons across the field reversal causes the formation of the electric field inversion layer and associated phase space hole.[22] On ion scales, the Hall effect causes charge separation and the formation of the well-known ion-scale potential well. The Hall potential well then accelerates ions towards the X-line, forming counter-streaming ion beams. These multi-scale reconnection features lead to non-Maxwellian distributions at the X-line which, for each species, can be well approximated by two distinct counter-streaming populations in the region where the magnetic field is weak.

The significant free energy available in these streaming populations can destabilize multistream instabilities. Multistream instabilities have been previously studied in the context of double-layers,[15] but the regimes previously studied are not applicable within the electron diffusion layer.

A. 1D linear model

As a model for the electron diffusion layer in the anti-parallel limit, we assume that the reduced ion and electron distribution functions, $f(x, v_x)$, can each be approximated by two Maxwellians drifting in the $\pm\hat{x}$ direction,

$$f_s(v_x,x) = \frac{n_0}{\sqrt{2\pi}v_{ths}}\left[\delta n \exp\left(-\frac{(v_x-U_s)^2}{2v_{ths}^2}\right) + (1-\delta n)\exp\left(-\frac{(v_x+U_s)^2}{2v_{ths}^2}\right)\right], \quad (1)$$

where δn is a parameter between 0 and 1 which determines the density asymmetry of the streaming populations. As shown in Figure 2, with the exception of the electron distribution function in the Harris sheet cases, this model approximates the distribution functions measured in the simulations well.

In general, n_0, v_{ths}, δn, and U_s are all dependent on x, however, the inhomogeneity length scale is the electron skin-depth. In the limit $c/v_{the} \to \infty$, the inhomogeneity is negligible for short wavelength modes and all parameters may be treated as spatially constant. Furthermore, the magnetic field is weak very near the X-line, so we assume the plasma is unmagnetized in this region. The reconnection electric field is in general not negligible, however, it is not essential in understanding the basic linear instability within the reconnection plane and so we neglect it.

Under these approximations, the linear dispersion relation for electrostatic modes is given by[30]

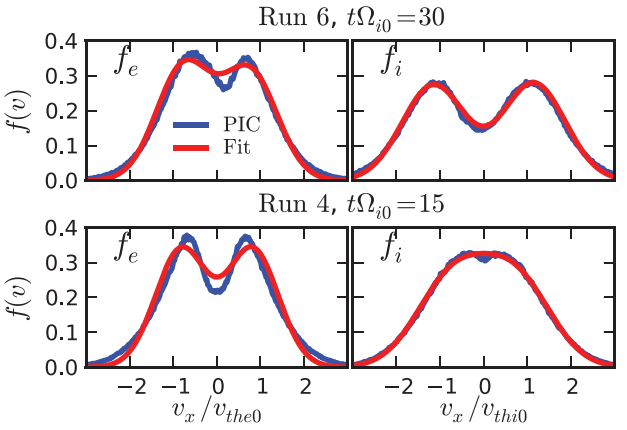

FIG. 2. In blue, the measured distribution functions near the X-line for cases 4 and 6, and in red the best fit to the model distribution function (1). The proposed model works well in most cases, however there is some discrepancy in modeling electrons in the Harris geometry.

$$2k^2 = \delta n Z_0'\left(\frac{\omega}{\sqrt{2}k} - \hat{U}_e\right) + (1-\delta n)Z_0'\left(\frac{\omega}{\sqrt{2}k} + \hat{U}_e\right) + \tau^2\left[\delta n Z_0'\left(\frac{\omega\mu\tau}{\sqrt{2}k} - \hat{U}_i\right) + (1-\delta n)Z_0'\left(\frac{\omega\mu\tau}{\sqrt{2}k} + \hat{U}_i\right)\right], \quad (2)$$

where Z_0 is that standard plasma dispersion function.[31] Here, the following dimensionless variables are used:

$$\omega/\omega_{pe} \to \omega \quad k\lambda_{De} \to k \quad \sqrt{m_i/m_e} \to \mu \quad U_e/\sqrt{2}v_{Te} \to \hat{U}_e \quad U_i/\sqrt{2}v_{Ti} \to \hat{U}_i \quad \sqrt{T_e/T_i} \to \tau \quad (3)$$

and ω_{pe} and λ_{De} are computed using the total density, n_0.

If we now specialize to the case of symmetric reconnection, then there should be zero net in-plane current near the X-line and all the beams should have approximately equal density, $\delta n = 1/2$. Stability boundaries and growth rates have been calculated for this case, and examples are given for $T_i = T_e$ in Figure 3. Within the parameter regime of interest, there are two unstable branches for this symmetric configuration. One, labeled $ee - ii$, is purely growing, while the other, labeled $e - i_{co}$ is a propagating mode.

In the limit of large drift velocities, the instability boundaries shown in Figure 3(a) are well approximated by those of standard two-stream instabilities. For two counter-streaming populations a and b with equal Debye lengths, $n_a T_b = n_b T_a$, the minimum relative drift velocity, V_d, required for instability is given by[15,32]

$$\frac{V_d}{\sqrt{2}v_{tha}} = 0.92\left(1 + \frac{\omega_{pb}}{\omega_{pa}}\right), \quad (4)$$

where ω_{pa} and v_{tha} are the plasma frequency and thermal velocity of species a. Similarly, ω_{pb} is the plasma frequency of species b. From this relation, the stability boundary for the purely growing mode is easily understood as the requirement that *both* the electron-electron two-stream instability ($a = b = e$) and the ion-ion two-stream instability ($a = b = i$) are unstable.

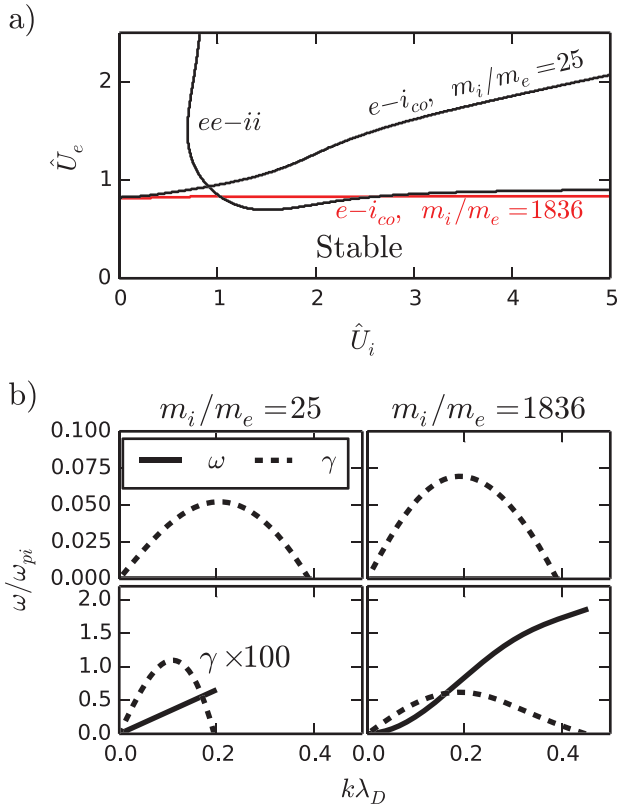

FIG. 3. (a) Stability boundaries for the parameter region of interest and $\tau = 1$. (b) Dispersion relation for the purely growing mode (top row) and the Buneman-like mode (bottom row), at the parameters $\hat{U}_e = \hat{U}_i = \tau = 1$, for both a reduced mass ratio and hydrogen mass ratio. Note that the growth rate of the Buneman-like mode at the reduced mass ratio is enhanced by a factor of 100 for clarity.

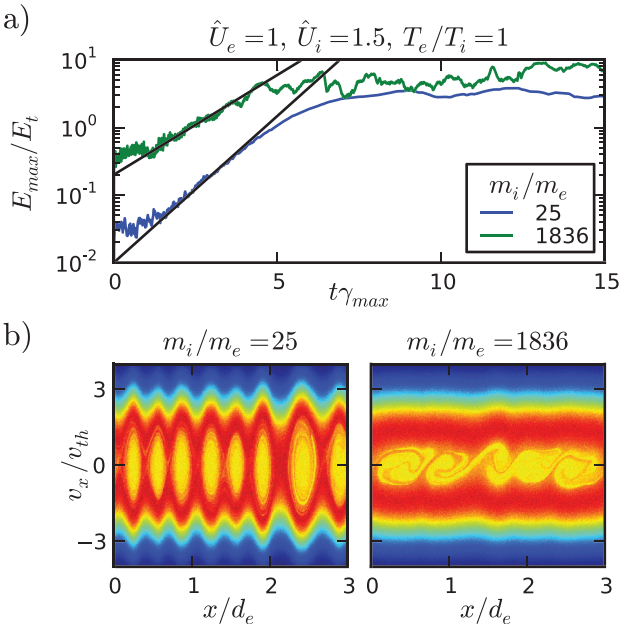

FIG. 4. Example 1D PIC simulations of the multistream instabilities, see text for parameters. (a) Peak electric field normalized to the electron trapping field for the fastest growing mode. Time is normalized to the fastest growth rate, and in black the linear growth rate for the dominant purely growing mode is shown. (b) Electron phase space contours after saturation occurs.

Likewise, the instability boundary for the propagating mode is found to be well approximated by the requirement that the co-moving electron and ion populations are unstable to the Buneman instability ($a = e$, $b = i$). For electron drifts well above the threshold, this mode becomes purely growing for long wavelengths, although this is not the parameter regime of interest here.

At low drift velocities, these approximations to the instability boundary break down since three- and four-stream interactions must be taken into account. This is the parameter regime relevant to the electron diffusion layer where typically $\hat{U}_e \sim 1$, $\hat{U}_i \gtrsim 1$. Example dispersion relations for the two modes at the parameters $\hat{U}_i = \hat{U}_e = 1$ are shown in Figure 3(b). There, the growth rate of the purely growing mode is set by the ion dynamics and so scales with ω_{pi}. In contrast, the Buneman-like mode has a growth rate which scales with ω_{pe}.

B. 1D nonlinear evolution

While it is well known that the 1D nonlinear evolution of two-stream instabilities generates phase space holes,[33,34] it is worthwhile to examine the nonlinear evolution of these multistream instabilities. Simple 1D simulations were performed in a short ($3d_e$) periodic box in order to exclude possible electromagnetic modes. Two examples at the parameters $\hat{U}_e = \tau = 1$, $\hat{U}_i = 1.5$, and $c/v_{the} = 64$ are shown in Figure 4 for both a reduced mass ratio and hydrogen mass ratio. The electric field is normalized to the electric field due to electron trapping, defined by[35,36]

$$E_t = \frac{m_e}{e}\left(\frac{32}{3\pi}\right)^2 \frac{\gamma_{max}^2}{k_{max}} \tag{5}$$

and time is normalized to the linear growth rate of the fastest growing mode.

For the hydrogen mass ratio case shown, the Buneman-like mode is the fastest growing mode, whereas at low mass ratio, only the purely growing mode is unstable. Despite this, the linear growth of both cases is well described by the fastest purely growing mode allowed. The saturated electric field is larger than that estimated by (5) since both ions and electrons provide free energy for the growing mode, but particle trapping is still the mechanism for saturation in these 1D cases.

In higher dimensions, the nonlinear evolution will be fundamentally different due to the possibility of quasilinear-diffusion in velocity space,[35] as well as detrapping of particles due to a finite length of these structures. For the two-stream instability, it has been shown that the saturated state of the instability does not have coherent phase space holes in 2D or 3D.[34] This result, however, is not directly applicable to the electron diffusion layer, where the geometry and boundary conditions are fundamentally different.

V. ONSET OF INSTABILITY

A. Dominant modes

Both the small scale structures shown in Figure 1 and the linear theory presented demonstrate that the characteristic wavelengths are of Debye scale. The typical wavenumber of

these modes is $k_x\lambda_D \sim 0.2$, consistent with both the linear theory predictions shown in Figure 3(b) and the simulation results, Figure 6(a). This implies the wavelength of these modes is approximately $30\lambda_D$. Now in order for this mode to be unstable, electrons are required to maintain their counter-streaming structure along the entire wavelength. If this were not the case, so that there was a significant electron population near the wave phase velocity (i.e., near $v_x = 0$), then this population would be free to screen out the growing space charge associated with the wave field. This would result in the wave being stabilized by electron Debye shielding.

The length scale of the electric field inversion layer and associated electron phase-space hole is determined by the electron meandering orbits, and so is of d_e scale,[22] although still smaller than the current layer width. This implies a minimum scale separation of $d_e/\lambda_D = c/v_{the} \gtrsim 30$ in order for instability to develop.

In order to test this prediction, we performed 4 simulations using the Harris geometry and kept all parameters fixed except for the electron temperature, see cases 1–4. Contours of both the electrostatic potential and the reduced electron phase space $f(x, v_x)$ at $z = 0$ are shown in Figure 5 for the time $t\Omega_{i0} = 20$. There is a clear bifurcation of the inversion layer into two distinct electron holes in case 3 and a further bifurcation into 4 electron holes in case 4. This is consistent with the predictions from linear theory and demonstrates that these modes are fundamentally of Debye scale. These multiple Debye scale electron holes are fundamentally different in that they are dynamic and can interact with each other to generate microturbulence within the layer.

Since these simulations are 2D, it is not possible for the turbulence to significantly alter the out-of-plane force balance via anomalous resistivity. As a result, both the reconnection rate and layer width are insensitive to c/v_{the}. Furthermore, the beam temperatures and drift speeds found by fitting the distribution function at the X-line to (1) are also independent of c/v_{the} above the instability threshold, so that the presence of multiple modes is due purely to increased scale separation rather than changing parameters.

B. Linear growth rates

Since the growth rates predicted by linear theory scale with the ion plasma frequency, whereas reconnection dynamics occur on the ion cyclotron time scale, the onset of these instabilities should be very rapid. A consequence of this is that from the perspective of studying reconnection dynamics, it is the saturated, nonlinear behavior that is of interest. Nevertheless, studying the linear onset of these instabilities is important in order to demonstrate the fundamental physics involved. Here, we consider two cases at $c/v_{the} = 64$, one in the MRX geometry (case 6) and one in the Harris geometry (case 4).

In case 6, linear theory predicts that instability should develop near the time range $t\Omega_{i0} = 30$–32, and using the measured distribution function at $t\Omega_{i0} = 32$, the dominant mode should be $k_x\lambda_{De0} = 0.17$ with a linear growth rate of $\gamma = 0.01\omega_{pi0}$. Background noise within the diffusion layer is significant enough to obscure the initial onset of instability,

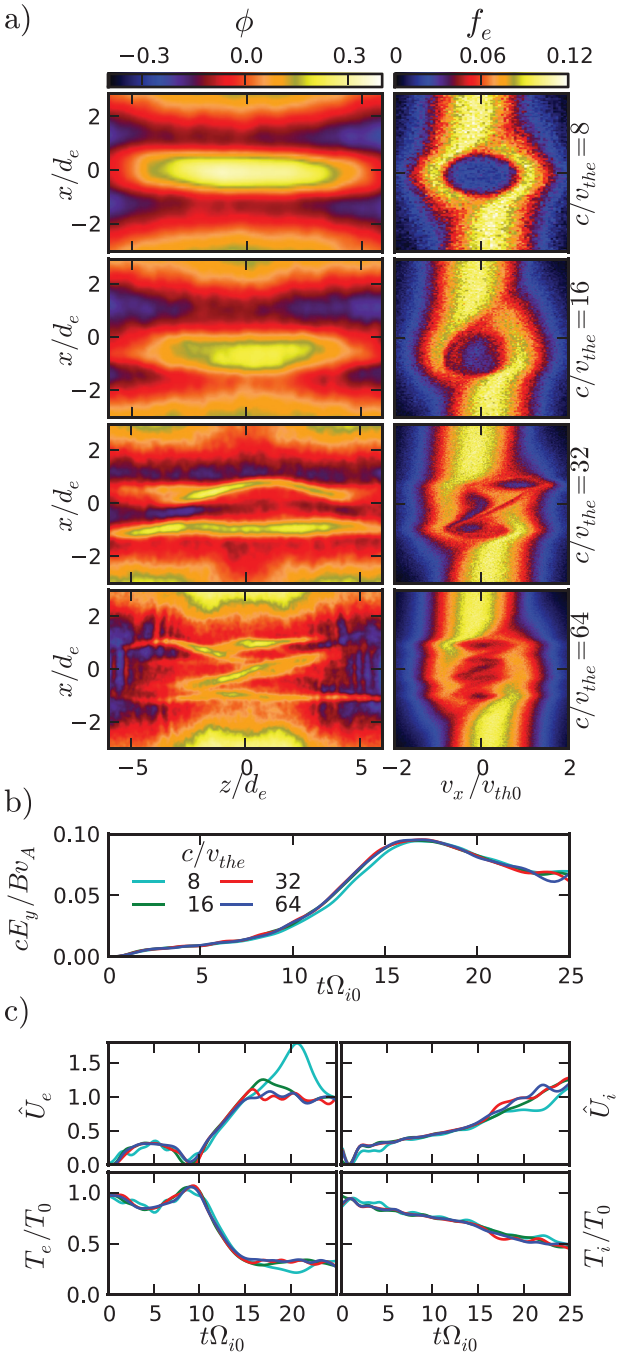

FIG. 5. Comparison of runs 1-4 (a) electrostatic potential and reduced electron phase space during the nonlinear phase. For easier comparison, a constant has been added to ϕ such that in the region shown the mean is zero. For runs 1 and 2, our results reproduce those of Chen *et al.*[22] Both the reconnection rate (b) and time averaged model parameters (c) are insensitive to c/v_{the}. The model parameters are computed by fitting the reduced distribution functions to (1) and are smoothed in time to remove transient fluctuations due to the motion of electron holes.

however once the electric field rises above this background at $t\Omega_{i0} = 32.5$, it grows with a growth rate matching that of linear theory almost exactly.

In case 4, our idealized model for the electron distribution function does not match the measured distribution function well, as shown in Figure 2, so we do not expect the linear theory presented to be as accurate. Well before the predicted onset of instability, there is clear growth of the

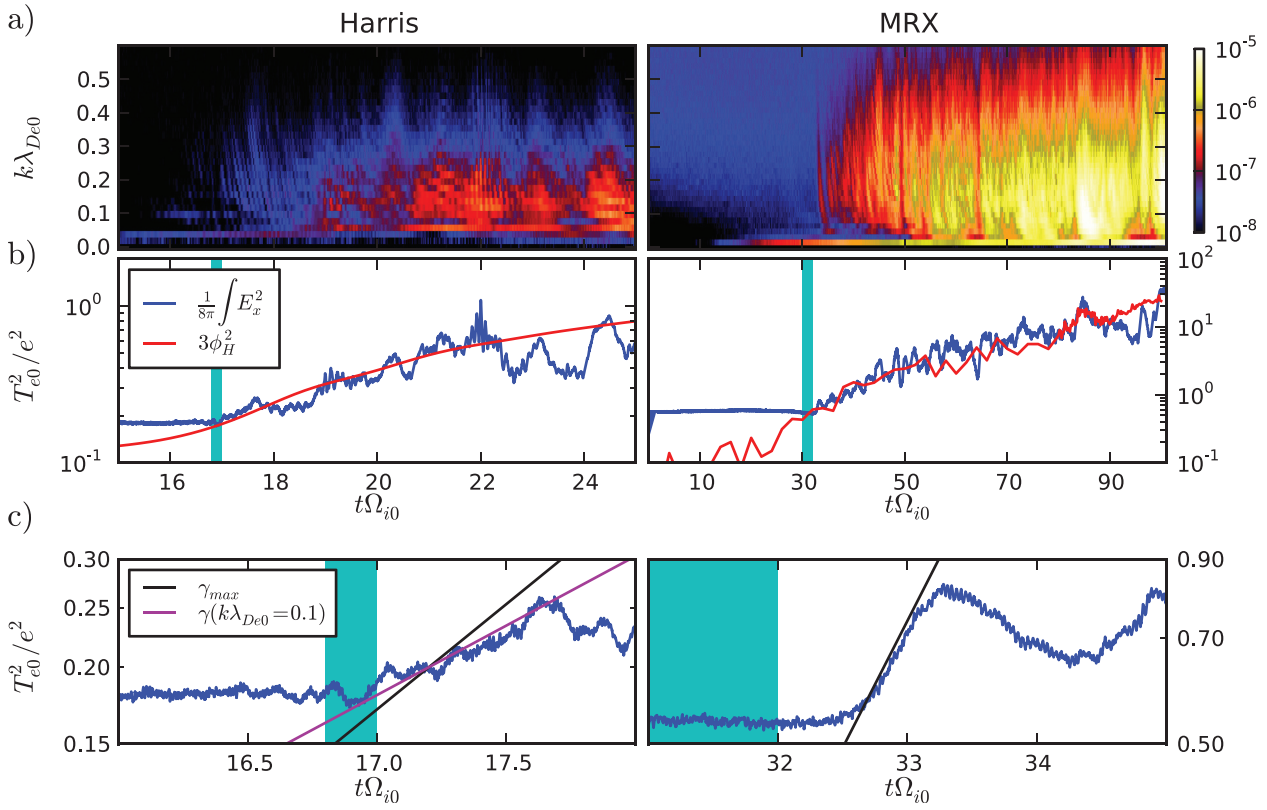

FIG. 6. Electric field energy within the diffusion layer due to the multistream instability. Here, the diffusion layer is defined as the box centered at the X-point with a half length of $5d_e$ and a half width of $3d_e$ for the MRX case (run 6) and $2.5d_e$ for the Harris case (run 4). (a) Wavenumber spectra as a function of time. (b) Total electric field energy contained within the diffusion layer and in modes with $k_x d_e \geq 1$. The time window during which the linear theory predicts multistream instabilities to become unstable is highlighted in teal. In red, the value of $3\phi_H^2$ is shown, where ϕ_H is the depth of the ion potential well, as discussed in Sec. VI A. (c) Electric field energy near the observed onset of instability. The growth rate of the fastest growing mode is shown in black, and the growth rate of the $k_x\lambda_{De0}=0.1$ mode is shown in purple.

$k_x\lambda_{De0}=0.1$ mode, see Figure 6(a), however, this does not translate into an increase in the total field energy within the diffusion layer. As shown in Figure 2, the electron distribution function in case 4 is not well modeled by (1), especially near $v_x=0$. More recently, we have used a more accurate model of the electron distribution function instead of (1), and have found additional unstable electron modes with growth rates on the order of the electron plasma frequency (not shown). It is likely that it is these modes which are responsible for the observed $k_x\lambda_{De0}=0.1$ fluctuations.

The simple model presented here predicts the onset of instability between $t\Omega_{i0} = 17 - 17.2$, which is consistent with the observed growth of the total field energy. Using the measured drift speeds and temperatures at $t\Omega_{i0}=17.2$, the maximum growth rate is $\gamma_{max} = 2.5\times10^{-3}\omega_{pi0}$, however this occurs at a long wavelength $k_x\lambda_{De0}=0.069$. Due to the inhomogeneities and the initial electron mode, the $k_x\lambda_{De0}=0.1$ mode is dominant, and so the energy growth should be determined by the slower growth rate of this mode, $\gamma = 1.6\times10^{-3}\omega_{pi0}$. As shown in Figure 6, this growth rate matches the observed growth rate well.

VI. NONLINEAR EVOLUTION

A. Saturation

Since the nonlinear saturation of these modes occurs shortly after onset, the amplitude of these modes on timescales relevant to reconnection is set by the nonlinear response. In 1D, the nonlinear saturated amplitude due to trapping is determined by Eq. (5), which, recalling that the linear growth rate scales with ω_{pi}, implies that the saturated amplitude decreases linearly with mass ratio.

In 2D, however, this does not appear to be the case, as Eq. (5) implies that saturated electron holes would be much smaller than those observed. Furthermore, Figure 7 shows that electron holes with comparable amplitudes are observed in both cases (6) and (7), so that mass ratio may not play an important role in determining the saturated amplitude of these modes. Here we argue that for the parameter regime studied, the nonlinear saturated amplitude is due to ion dynamics, and is set by the depth of the ion-scale potential well responsible for driving the counter-streaming ions.

In order to maintain a potential hill with amplitude ϕ_0 and width L, a net space charge must be maintained at the center of the electron hole.

$$\rho_0 = e(n_i - n_e) \approx \frac{\phi_0}{4\pi L^2}. \tag{6}$$

On electron timescales, ions are static so n_i is constant and this constraint leads to the width-amplitude inequality for electron holes.[37] However, on ion timescales, n_i may vary. In the electron diffusion layer, ions are continually exhausted into the outflow and are replenished by the inflowing ion beams. If the ion beams are of lower energy than $e\phi_0$, then

ions are fully reflected and cannot penetrate into the electron hole. Then, due to the loss of ions to the exhaust, the amplitude will decay. The energy of the ion beams is set by the Hall electric fields, so on ion timescales the scaling $\phi_0 \sim \phi_H$ should hold. This suggests that the total field energy contained in a single electron hole should scale as

$$\frac{E_x^2}{8\pi} \sim \frac{\phi_0^2}{L^2} \sim \frac{\phi_H^2}{L^2}. \tag{7}$$

As shown in Figure 6(b), this scaling holds in the two cases considered and is expected to hold provided that the saturated amplitude due to electron physics is larger than the potential well depth. Here the potential well depth is directly measured at $z = 0$, by taking the difference between the maximum ϕ located between 0.5 and $1d_i$ upstream and the minimum ϕ between $\pm 0.5 d_i$.

Under an assumption of quasi-steady state, the in-plane potential can be estimated by integrating Ohm's law along the inflow. Here, we make a distinction between the ion-scale Hall potential well and the electron scale potential structures, and so we begin integrating from the edge of the electric field inversion layer, roughly at $x = d_e$, rather than from the X-point. As a result, electron inertia terms are negligible and so

$$\frac{e\phi_H}{T_e} = -\frac{1}{T_e}\int_{d_e}^{d_i} \frac{1}{n_e}\left(\frac{J_y B_z}{c} - [\nabla \cdot \mathbf{P_e}]_x\right) dx. \tag{8}$$

In the limit of a diagonal pressure tensor, the role of the pressure tensor term is to remove the effects of diamagnetic drift.[38] Under the additional assumptions of uniform density and massive ions, the Hall potential well depth is given by[39]

$$\frac{e\phi_H}{T_e} = \frac{1}{\beta_e} + \frac{\Delta T_e}{T_e}, \tag{9}$$

where ΔT_e is the change in electron temperature across the inflow region. Although this formula was experimentally tested and shown to hold,[39] this is not expected to hold exactly in kinetic simulations where density is not uniform throughout the inflow and the pressure tensor has off-diagonal terms. Nevertheless, this formula suggests that the Hall potential well depth will be larger and this instability will be stronger at lower values of β_e; again provided that saturation is determined by ion physics and not by electron physics. This is consistent with our results where case 6 has a larger potential well, lower value of β_e, and a significantly stronger instability than case 4.

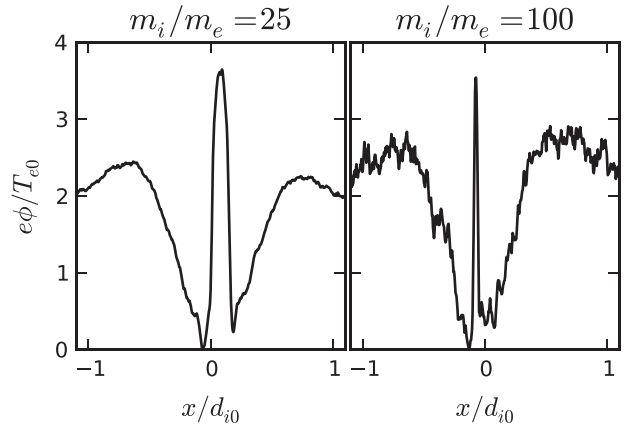

FIG. 7. Electrostatic potential at $z = 0$ and $t\Omega_{i0} = 86$ for cases 6 and 7. Large amplitude electron holes are still present at $m_i/m_e = 100$.

B. Particle trapping

Due to the presence of both large amplitude and small scale electron holes, intense electric fields are present within the diffusion layer. These electric fields can trap particles within the electron holes, leading to the formation of localized regions with significantly enhanced particle and current density. Furthermore, continual acceleration of trapped particles by the reconnection electric field reinforces the current density perturbation, leading to a very intense out-of-plane current. This localized current spike can be as large as twice the background current in some cases. An example of such a perturbation is shown in Figure 8.

Despite the intense currents generated, the perturbations do not directly affect the magnetic field topology. This is counter-intuitive since one would expect that these localized current spikes should in fact form small-scale, topologically distinct islands. In fact, recent measurements in MRX have shown that magnetic islands or flux ropes exist down to scales below the layer thickness.[6] However, in order to form islands, new null-lines must be formed. This places a constraint on the size of the perturbations and the current density required in order to form islands, and this constraint is not met in our current 2D simulations which all employed artificial mass ratios in the range $m_i/m_e = 25$–100. However, it is

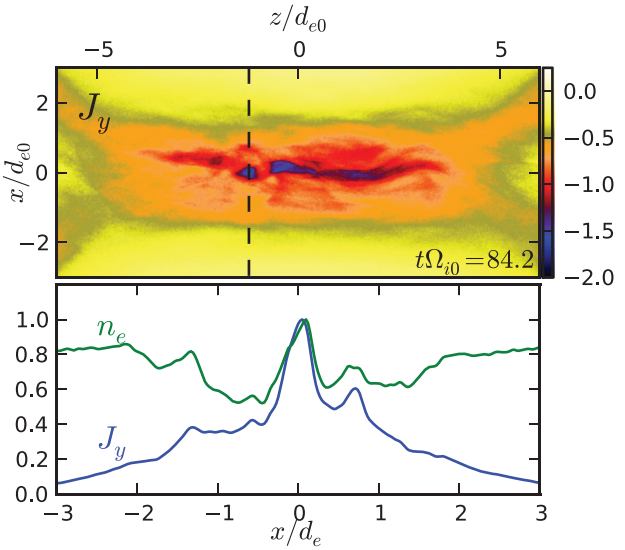

FIG. 8. Intense current perturbations are associated with electron trapping in Debye scale electron holes. Top: out-of plane current density normalized to the initial electron thermal speed, taken from case 6. Bottom: electron density and current density along the illustrated cut, both normalized to peak values. Note that unlike Harris profiles, current sheets generated within the MRX geometry typically have hollow density profiles, and this is not an effect of the instability.

possible that in 3D, and with realistic parameters, these fluctuations could seed the formation of flux ropes.

Even if flux ropes are not produced by this instability, the ability to trap particles in small-scale electrostatic structures rather than magnetic structures is interesting in its own right. Many existing theories for particle acceleration during magnetic reconnection rely on trapping in magnetic islands[40,41] and may also be applicable to particles trapped in small-scale electrostatic structures. Such an investigation is, however, beyond the scope of the current work.

VII. COLLISIONAL EFFECTS

All of the simulations above are collisionless, and are of direct applicability to the magnetosphere, but the real MRX experiment has finite collisionality. For this instability to be relevant in explaining experimental observations, the role of finite collisionality must be examined.

Formally, the criteria for the validity of the collisionless Vlasov equation is given by[30]

$$(k\lambda_{mfp})^{1/3} \gg 1. \tag{10}$$

Using the typical MRX parameters listed in Table I gives that $\lambda_{mfp,e}/\lambda_D = \omega_{pe}/\nu_{ee} \sim 3500$, and thus in MRX the collisionless Vlasov equation is valid for modes satisfying

$$(k\lambda_D)^{1/3} \gg 0.066. \tag{11}$$

This suggests that collisional modifications to the linear evolution of these modes are not large. A more serious restriction comes from the accessibility of these modes under finite collisionality. Specifically, since both ion scale and electron scale dynamics are necessary in order to generate the initially unstable distributions, even weak collisionality may be sufficient to prevent the unstable distributions of the type in (1) from forming.

In order to test the accessibility of these modes under weak collisionality, we have performed a series of simulations in the MRX geometry using a standard algorithm to model the Landau collision operator[42,43] using the explicit particle in cell code VPIC.[44,45] These simulations were performed at a high thermal speed $c/v_{the} = 8$, and at two different mass ratios $m_i/m_e = 100$, 400 and values of $\beta_0 = 1/16$ 1/32. While these simulations are expected to be stable due to a lack of scale separation, they can be used to diagnose the accessibility of these instabilities by examining the normalized in-plane drift speeds at the X-point, $\hat{U}_e$ and $\hat{U}_i$.

For the parameters chosen, $\hat{U}_i$ is always large, such that the stability threshold is approximately that of the electron two-stream instability, namely $\hat{U}_e \geq 0.92$. We have empirically found that the parameter $\hat{U}_e$ depends only on the dimensionless quantity $E/(E_D\beta_e^\star)$. Here the superscript $\star$ is used to denote quantities computed using the reconnecting magnetic field at 1 δ (current-sheet half-width) upstream and densities and temperatures measured at the center of the current sheet, and E_D is the Dreicer electric field given by

$$E_D = \frac{m_e}{e}\nu_e v_{the}. \tag{12}$$

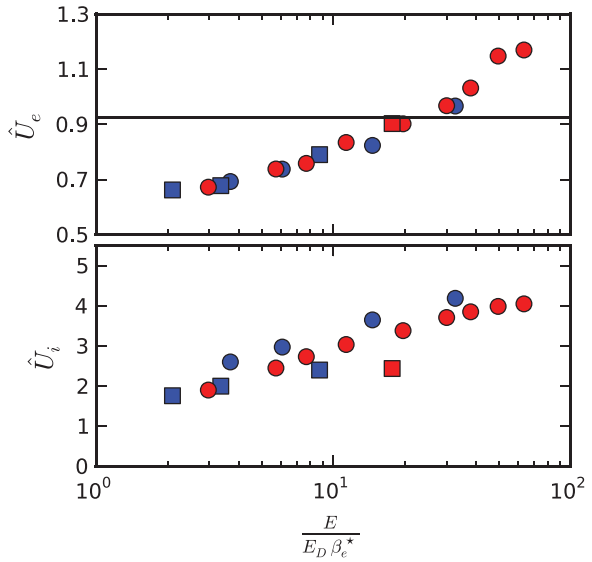

FIG. 9. Results of collisional simulations. Blue data points have $m_i/m_e = 400$, red points have $m_i/m_e = 100$. Squares have $\beta_0 = 1/16$ and circles have $\beta_0 = 1/32$.

The results from these collisional cases are shown in Figure 9. For reference, MRX discharges have been reported with $E/(E_D\beta_e^\star) \sim 100$, however, these are achieved only through very low $\beta_e^\star$ and a spatially varying guide-field.[6] More typical discharges in MRX have $E/(E_D\beta_e^\star) \sim 5$, well below the stability threshold found in this study.[6,39]

While these results suggest that a majority of MRX experiments are stable, we would caution that applicability of these results to the MRX experiment is not clear. Fundamentally, these simulations still do not agree with experimental measurements of force balance and electron layer width.[5,6,9] As a result, the effect of a broad diffusion layer on the accessibility of these modes is unknown.

The impact of these discrepancies on our results is not negligible. For instance, in the simulations, the curl-free vacuum field is not small compared to the reconnecting magnetic field and so the normalization convention used here includes the vacuum field in the calculation of $\beta_e^\star$. In the experiments, however, the vacuum component is negligible and so it is not included in $\beta_e^\star$. Including only the reconnecting magnetic field in our normalization would shift all of the above data points to the left by roughly a factor of 2. This alone is not sufficient to bring the typical MRX discharge into the unstable region, but instead demonstrates one possible way in which the predicted stability boundary can be modified.

While the accessibility of these modes in current generation reconnection experiments is questionable, future experiments, such as those suggested by Ji and Daughton,[20] will be able to reach the lower collisionalities needed to access these modes.

VIII. DISCUSSION

Here, we have presented evidence for the presence of Debye scale electrostatic turbulence within the electron

diffusion layer. Previous work has shown that 3D electrostatic turbulence can be generated via parallel streaming instabilities,[16] and that such turbulence can affect electron heating within the diffusion layer. This work is fundamentally different from these out-of-plane instabilities in that the instabilities discussed here are due to in-plane, cross-field streaming in a region of weak magnetic field. Furthermore, unlike streaming instabilities on the separatrices,[17] these instabilities are localized within the diffusion layer where the presence of significant anomalous resistivity is needed in order to explain experimental observations. Finally, unlike all other previous discussions on streaming instabilities during reconnection, this instability does not require a guide field in order to operate. Preliminary work suggests that in 2D very weak guide fields of above 5% of the reconnecting magnetic field act to suppress this instability. This is consistent with previous simulations which showed the disappearance of the electric field inversion layer with weak guide fields.[46]

The fundamental mechanism for instability is a multi-stream instability due to the interaction of the electron-electron and ion-ion two stream instabilities. The ions play the major role, setting both the growth rate and, for the cases studied here, the saturated amplitude of the generated electron holes. These unstable distributions are naturally generated during active, collisionless reconnection both in the idealized Harris geometry and in the driven current sheets present in the MRX geometry. Thus, this instability seems to be a general feature of anti-parallel, collisionless reconnection in the cool ($T_e \lesssim 500\,\mathrm{eV}$) limit.

The nonlinear evolution of these instabilities generates multiple Debye scale electron holes localized within the electron diffusion layer. While electron holes have been observed both in space[47] and in laboratory experiments,[21] none of these observations have been within an active electron diffusion layer during anti-parallel reconnection and so cannot be directly compared with the predictions made here.

Particle trapping within electron holes leads to intense, localized current perturbations within the diffusion layer. While such perturbations are relatively passive in 2D, secondary instabilities could be generated due to these perturbations in 3D. In particular, it seems plausible that they could be sites of particle acceleration and the seeds for small-scale flux ropes.

Fundamentally, our results demonstrate that the internal structure of the diffusion layer may not be laminar in the parameter regimes relevant to reconnection in the magnetosphere. With the upcoming launch of MMS, collisionless electron physics will be an important area of focus, but understanding and interpreting MMS data may require fully kinetic modeling with realistic scale separation between the electron skin depth and the Debye length.

ACKNOWLEDGMENTS

It is a pleasure to acknowledge fruitful discussions with Li-Jen Chen. This work was supported in part by the DOE under contract number DE-AC02-09CH11466 and by the NASA Geospace Science Program under Grant Number NNH10A0471. Contributions from W.D. are supported by NASA's Heliophysics Theory Program. Simulations were performed using Los Alamos National Laboratory Institutional Computing and on Blue Waters which is supported by the NSF (OCI 07-25070) and the State of Illinois.

[1]M. Yamada, R. Kulsrud, and H. Ji, Rev. Mod. Phys. **82**, 603 (2010).
[2]J. Birn, J. F. Drake, M. A. Shay, B. N. Rogers, R. E. Denton, M. Hesse, M. Kuznetsova, Z. W. Ma, A. Bhattacharjee, A. Otto *et al.*, J. Geophys. Res.: Space Phys. **106**, 3715 (2001).
[3]Y. Ren, M. Yamada, S. Gerhardt, H. Ji, R. Kulsrud, and A. Kuritsyn, Phys. Rev. Lett. **95**, 055003 (2005).
[4]M. Yamada, Y. Ren, H. Ji, J. Breslau, S. Gerhardt, R. Kulsrud, and A. Kuritsyn, Phys. Plasmas **13**, 052119 (2006).
[5]S. Dorfman, W. Daughton, V. Roytershteyn, H. Ji, Y. Ren, and M. Yamada, Phys. Plasmas **15**, 102107 (2008) .
[6]S. E. Dorfman, Ph.D. thesis, Princeton University, 2012.
[7]S. Dorfman, H. Ji, M. Yamada, J. Yoo, E. Lawrence, C. Myers, and T. D. Tharp, Geophys. Res. Lett. **40**, 233, doi:10.1029/2012GL054574 (2013) .
[8]H. Ji, Y. Ren, M. Yamada, S. Dorfman, W. Daughton, and S. P. Gerhardt, Geophys. Res. Lett. **35**, L13106, doi:10.1029/2008GL034538 (2008).
[9]V. Roytershteyn, S. Dorfman, W. Daughton, H. Ji, M. Yamada, and H. Karimabadi, Phys. Plasmas **20**, 061212 (2013).
[10]S. Dorfman, H. Ji, M. Yamada, J. Yoo, E. Lawrence, C. Myers, and T. Tharp, Phys. Plasmas **21**, 012109 (2014).
[11]J. D. Scudder, R. D. Holdaway, W. S. Daughton, H. Karimabadi, V. Roytershteyn, C. T. Russell, and J. Y. Lopez, Phys. Rev. Lett. **108**, 225005 (2012).
[12]F. S. Mozer, S. D. Bale, and T. D. Phan, Phys. Rev. Lett. **89**, 015002 (2002).
[13]T. Moore, J. Burch, W. Daughton, S. Fuselier, H. Hasegawa, S. Petrinec, and Z. Pu, J. Atmos. Sol.-Terrestrial Phys. **99**, 32 (2013), http://www.sciencedirect.com/science/article/pii/S1364682612002611.
[14]O. Buneman, Phys. Rev. **115**, 503 (1959).
[15]V. Lapuerta and E. Ahedo, Phys. Plasmas **9**, 3236 (2002).
[16]H. Che, J. F. Drake, M. Swisdak, and P. H. Yoon, Geophys. Res. Lett. **37**, L11105, doi:10.1029/2010GL043608 (2010).
[17]M. V. Goldman, D. L. Newman, and P. Pritchett, Geophys. Res. Lett. **35**, L22109, doi:10.1029/2008GL035608 (2008).
[18]J. R. Wygant, C. A. Cattell, R. Lysak, Y. Song, J. Dombeck, J. McFadden, F. S. Mozer, C. W. Carlson, G. Parks, E. A. Lucek *et al.*, J. Geophys. Res.: Space Phys. **110**, A09206 (2005).
[19]T. D. Phan, J. T. Gosling, M. S. Davis, R. M. Skoug, M. Øieroset, R. P. Lin, R. P. Lepping, D. J. McComas, C. W. Smith, H. Reme *et al.*, Nature **439**, 175 (2006).
[20]H. Ji and W. Daughton, Phys. Plasmas **18**, 111207 (2011).
[21]W. Fox, M. Porkolab, J. Egedal, N. Katz, and A. Le, Phys. Rev. Lett. **101**, 255003 (2008).
[22]L.-J. Chen, W. S. Daughton, B. Lefebvre, and R. B. Torbert, Phys. Plasmas **18**, 012904 (2011).
[23]G. Lapenta, S. Markidis, A. Divin, M. Goldman, and D. Newman, Phys. Plasmas **17**, 082106 (2010).
[24]A. Divin, G. Lapenta, S. Markidis, D. L. Newman, and M. V. Goldman, Phys. Plasmas **19**, 042110 (2012).
[25]H. Karimabadi, V. Roytershteyn, M. Wan, W. H. Matthaeus, W. Daughton, P. Wu, M. Shay, B. Loring, J. Borovsky, E. Leonardis *et al.*, Phys. Plasmas **20**, 012303 (2013).
[26]W. Daughton, Phys. Plasmas **9**, 3668 (2002).
[27]V. Roytershteyn, W. Daughton, S. Dorfman, Y. Ren, H. Ji, M. Yamada, H. Karimabadi, L. Yin, B. J. Albright, and K. J. Bowers, Phys. Plasmas **17**, 055706 (2010).
[28]M. Yamada, H. Ji, S. Hsu, T. Carter, R. Kulsrud, N. Bretz, F. Jobes, Y. Ono, and F. Perkins, Phys. Plasmas **4**, 1936 (1997).
[29]D. Forslund, Space Sci. Rev. **42**, 3 (1985) .
[30]T. H. Stix, *Waves in Plasmas* (Springer, 1992).
[31]B. D. Fried and S. D. Conte, *The Plasma Dispersion Function* (Academic, New York, 1961).
[32]E. A. Jackson, Phys. Fluids **3**, 786 (1960).
[33]K. V. Roberts and H. L. Berk, Phys. Rev. Lett. **19**, 297 (1967).
[34]R. L. Morse and C. W. Nielson, Phys. Rev. Lett. **23**, 1087 (1969).
[35]R. Z. Sagdeev and A. A. Galeev, *Nonlinear Plasma Theory*, (Benjamin, New York, 1969).
[36]K. Lotov, A. Terekhov, and I. Timofeev, Plasma Phys. Rep. **35**, 518 (2009),

[37]L.-J. Chen, J. Pickett, P. Kintner, J. Franz, and D. Gurnett, J. Geophys. Res., [Space Phys.] **110**, A09211 doi:10.1029/2005JA011087 (2005).
[38]D. A. Uzdensky and R. M. Kulsrud, Phys. Plasmas **13**, 062305 (2006).
[39]J. Yoo, Ph.D. thesis, Princeton University, 2013.
[40]J. F. Drake, M. Swisdak, H. Che, and M. A. Shay, Nature **443**, 553 (2006).
[41]M. Oka, M. Fujimoto, I. Shinohara, and T. D. Phan, J. Geophys. Res., [Space Phys.] **115**, A08223 doi:10.1029/2010JA015392 (2010).
[42]T. Takizuka and H. Abe, J. Comput. Phys. **25**, 205 (1977), http://www.sciencedirect.com/science/article/pii/0021999177900997.
[43]W. Daughton, V. Roytershteyn, B. J. Albright, H. Karimabadi, L. Yin, and K. J. Bowers, Phys. Plasmas **16**, 072117 (2009).
[44]K. Bowers, B. Albright, B. Bergen, L. Yin, K. Barker, and D. Kerbyson, in *International Conference for High Performance Computing, Networking, Storage and Analysis, 2008* (IEEE, 2008), pp. 1–11.
[45]K. J. Bowers, B. J. Albright, L. Yin, B. Bergen, and T. J. T. Kwan, Phys. Plasmas **15**, 055703 (2008).
[46]J. Ng, J. Egedal, A. Le, and W. Daughton, Phys. Plasmas **19**, 112108 (2012).
[47]C. Cattell, J. Dombeck, J. Wygant, J. F. Drake, M. Swisdak, M. L. Goldstein, W. Keith, A. Fazakerley, M. André, E. Lucek *et al.*, J. Geophys. Res., [Space Phys.] **110**, A01211 doi:10.1029/2004JA010519 (2005).